A Local Model for Planetary Atmospheres Forced by Small-Scale Convection

K. SHAFER SMITH

Center for Atmosphere Ocean Science, Courant Institute of Mathematical Sciences, New York University, New York, New York

(Manuscript received 29 May 2003, in final form 14 January 2004)

ABSTRACT

An equivalent-barotropic fluid on the β plane, forced at small scales by random stirring and dissipated by linear heat and vorticity drag, is considered as a local model for flow in the weather layer of internally forced planetary atmospheres. The combined presence of β, a finite deformation scale, and large-scale dissipation produce novel dynamics with possible relevance to the giant gas planets, which are apparently driven by small-scale convective stirring. It is shown that in order for anisotropy to form, one must have $\beta(\epsilon\lambda^5)^{-1/3} \gtrsim 3.9$, where ϵ is the (convectively driven) energy generation rate, λ is the deformation wavenumber, and β is the Coriolis gradient. The critical value above is not equivalent to the barotropic stability criterion, and numerical simulations demonstrate that anisotropic flow with average zonal velocities that are supercritical with respect to the latter can form. The formation of jets (a different matter) is not implied by the excess of zonal kinetic energy, and is instead sensitive to the relevant stability criterion for the flow geometry at hand. When β is sufficiently large that anisotropy does form, the flow scale and rms zonal velocity are set by a combination of Rossby wave cascade inhibition, the total energy constraint imposed by the large-scale dissipation, and the partitioning between available potential and kinetic energies. The resulting theory demonstrates that a relatively narrow range of parameters will allow for the formation of anisotropic flow with scale larger than the deformation scale. This is consistent with observations that indicate little separation between the jet scales and deformation scales on Jupiter and Saturn.

1. Introduction

Explanations of the basic features of Jovian circulation have ranged from deep convective rolls to baroclinic instability. Recently, based on analysis of data from the *Galileo* satellite, Gierasch et al. (2000) and Ingersoll et al. (2000) have argued that small-scale shallow convection from internally generated heat is widespread and likely represents the largest source of energy to the circulation. The organizing principle invoked is that of an inverse cascade of energy in two-dimensional barotropic vorticity flow, halted at the Rhines scale, resulting in the large-scale zonal jets observed. The implied model is similar to that of Williams (1978), but his model assumed forcing by baroclinic instability. Application of the Charney–Stern criterion to the observed jets on Jupiter and Saturn shows that they are barotropically unstable (Ingersoll and Pollard 1982), but nevertheless long-lived. Explanations of the stability of the jets range from a modified Charney–Stern criterion for deep flows (Ingersoll and Pollard 1982), noting that the observed jets are stable with respect to Arnold's Second Stability criterion (Dowling 1994), and a recent suggestion that a barotropic criterion modified to include friction could be satisfied by Jovian jets (Galperin et al. 2001). Numerical simulations of forced two-dimensional β-plane turbulence typically produce steady multiple-jet solutions only when large-scale dissipation is also present. In the absence of large-scale dissipation, jets continually merge until reaching the domain scale, both on the torus and on the sphere (Cho and Polvani 1996; Chekhlov et al. 1996; Manfroi and Young 1999; Huang et al. 2001; Smith et al. 2002). Moreover, the resulting jets are barotropically stable (Vallis and Maltrud 1993; Huang et al. 2001). A second characteristic of the observed jets is that the jet scale is not much larger than the deformation scale (Allison 2000), but the dynamical basis for this observation has not yet been explained.

Both two-dimensional β-plane turbulence on the one hand, and equivalent-barotropic turbulence on the other are relatively well-understood, while the combined effects of a finite deformation scale and β, both of which are nonnegligible in Jovian dynamics, have received only recent attention (Cho and Polvani 1996; Kukharkin and Orszag 1996; Okuno and Masuda 2003). Both parameters are fundamental to a wide range of phenomena in geophysical fluids. Moreover, the resulting dynamics of the combined system are nontrivial. For example, while β foments the formation of multiple jets, Okuno and Masuda (2003) demonstrate that a finite radius of

Corresponding author address: K. Shafer Smith, Center for Atmosphere Ocean Science, New York University, 251 Mercer Street, New York, NY 10012.
E-mail: shafer@cims.nyu.edu

deformation can suppress jet formation in freely evolving flow. The additional effects of small-scale forcing and large-scale drag further complicate the problem, but not so much as to make it intractable.

Kukharkin and Orszag (1996) demonstrate that adding a finite deformation scale to a stable-jet dominated flow can destabilize jets and produce vortices of slightly larger size than the deformation scale. Those authors did not produce a statistically steady state, however, since no large-scale dissipation was present, so little can be said about the jet scale they observed. They also introduced a second β-induced nonlinearity to the equations of motion, which, they argue, leads to a more relevant model. This term leads, in their simulations, to a preponderance of anticyclonic vortices, but this is not relevant to the balances that yield observed jet scales.

Huang et al. (2001) and Galperin et al. (2001) consider small-scale random forcing of two-dimensional vorticity dynamics on the sphere, with β and a large-scale hypofriction (∇^{-12} operator). However, no finite deformation scale is included, and the hypofriction is known to distort the cascade at long times and large scales (Borue 1994; Danilov and Gurarie 2001). The model is sufficiently complex to produce a k_y^{-5} spectrum, and Galperin et al. (2001) show that this is indeed the spectrum of the observed jets on Jupiter. The scale of their jets, however, was fit to the data by choosing an appropriate hypofriction coefficient.

The present work seeks to develop the turbulence phenomenology that applies when all of the major parameters affecting the large-scale circulation are present. However, both in the theory derived and in the numerical simulations used to test that theory, we neglect the effects of spherical geometry, dynamics precluded by the quasigeostrophic approximation, vertical variations in mean stratification and the explicit details of convection. Because we neglect spherical geometry from the outset, the present study does not address the global circulation problem in one pass. Instead, the familiar equivalent-barotropic model equation is taken to represent local patches of the global circulation, and hence fixed values of Coriolis gradient β and deformation wavenumber λ. By considering the latitudinal variations of these parameters, the results can be extrapolated to the globe. On can criticize the relevance of this approach to planetary circulation from the outset as being far too simplified, but it nevertheless addresses the problem of the interaction of parameters of the large scale circulation (β, λ, drag and energy generation) not yet explored, and so the simplicity of the geometry might be considered a prerequisite for this study.

In section 2 we derive a criterion necessary for the formation of flow anisotropy, and two candidate theories for the flow scale and rms zonal velocity. Limitations to the theories are also discussed. In section 3 we describe a large set of simulations performed to test the proposed theories. The simulations lead to a clear conclusion about which theory best describes the results. In section 4 we attempt to apply the theory to data for Jupiter and Saturn. Finally, in section 5 we discuss implications of the results.

2. Theory

a. Model formulation

The barotropic vorticity equation is written

$$\frac{\partial q}{\partial t} + J(\psi, q) = F + D - rq, \tag{2.1}$$

where ψ is the barotropic streamfunction,

$$q = \nabla^2\psi - \lambda^2\psi + \beta y \tag{2.2}$$

is the potential vorticity, λ is the deformation wavenumber, and r is a potential vorticity drag (a single inverse time scale that parameterizes both thermal and vorticity drag—lifting of this restriction will be considered later in the text). We shall assume that F represents a random forcing (be it a parametrization of stirring by interaction with baroclinic modes, or small-scale convection) confined to a scale κ_F^{-1}, and D is an enstrophy dissipation operator that acts only on wavenumbers $\kappa > \kappa_F$.

The net energy generation rate, less that unavoidably absorbed by the enstrophy dissipation, is

$$g \equiv \left\langle \int_A - \psi(F + D)\, da \right\rangle,$$

where $\langle\ \rangle$ denotes a time average, A is the domain area, and da is a differential area element. In this system, at scales smaller than the deformation scale, kinetic (K) and available potential (P) energy both cascade to larger scale. At scales larger than the deformation scale, P continues to cascade toward larger scale, while K does not. (If a large-scale source of kinetic energy exists, kinetic energy will cascade toward smaller scale, until it reaches the deformation scale). In numerical simulations, we shall equate the energy ($K + P$) generation rate with the upscale spectral transfer rate $\epsilon = g$, and hereafter refer only to ϵ.

Multiplying (2.1) by $-\psi$ and integrating to form an energy budget equation then reveals that the total statistically equilibrated energy is exactly

$$E = \frac{\epsilon}{2r}, \tag{2.3}$$

independent of β and λ (see, e.g., Smith et al. 2002). While linear vorticity drag may have limited applicability to atmospheric dynamics, the dissipation of heat implied by linear dissipation of potential vorticity in (2.1) is relatively physical. Furthermore, since available potential energy dominates kinetic energy at large scales, this part of the dissipation is the more crucial of the two for the present study.

A quadratic drag on vorticity is a more realistic parameterization of atmospheric dissipation. While no exact theory exists for total energy with a combination of linear heat dissipation and quadratic vorticity drag, its value can be estimated, and the prior and following arguments accordingly altered, but this avenue will not be pursued here. See Grianik et al. (2004) for a treatment of the effects of quadratic vorticity drag on the inverse barotropic cascade.

Smith et al. (2002) investigated the turbulence phenomenology of a similar system to that described here, but without β (as well as systems with $\beta \neq 0$ and $\lambda = 0$), and found that at scales large compared to the deformation scale, a linear drag on potential vorticity will act to yield a peak in the energy spectrum at

$$\kappa_r = (\alpha^3 r^3 \lambda^6 \epsilon^{-1})^{1/8}, \tag{2.4}$$

where $\alpha \equiv 27\mathcal{C}/44$, and $\mathcal{C}$ is the Kolmogorov constant. Defining a length scale and time scale

$$L = \lambda^{-1}, \qquad T = (\lambda^2 \epsilon)^{-1/3}, \tag{2.5}$$

we can rewrite (2.4) as

$$\kappa_r/\lambda = (\alpha \tilde{r})^{3/8}, \tag{2.6}$$

where $\tilde{r} = r(\lambda^2 \epsilon)^{-1/3}$. The addition of β to the dynamics, if sufficiently large, will lead to anisotropic flow. The critical value of β necessary for anisotropy to develop is derived next.

b. Necessary conditions for anisotropic flow

Equivalent-barotropic Rossby waves have the dispersion relation

$$\omega_R(k, l) = -\frac{k\beta}{k^2 + l^2 + \lambda^2}, \tag{2.7}$$

[where $\mathbf{k} = (k, l)$ is the two-dimensional wavenumber], which vanishes at the largest scale, in distinction from its barotropic counterpart, whose frequency is unbounded as $\boldsymbol{\kappa} \to 0$, where $\kappa = |\boldsymbol{\kappa}|$.

Assuming a constant stirring at small scales, and an ensuing upscale cascade of energy (total energy for $\kappa > \lambda$ and available potential energy for $\kappa < \lambda$), the turbulent straining rate in the Kolmogorov theory is

$$\tau^{-1}(|\boldsymbol{\kappa}|) = \mathcal{C}^{1/2} \epsilon^{1/3} |\boldsymbol{\kappa}|^{2/3}. \tag{2.8}$$

Anisotropy will begin to develop at scales larger than that at which the turbulent straining rate is equal to the Rossby wave frequency (Maltrud and Vallis 1991). One can see immediately that the curves represented by (2.7) and (2.8) will not intersect unless β is large enough, or ϵ or λ is small enough (see Fig. 1).

For critical parameters, a single intersection between (2.7) and (2.8) will occur along the $l = 0$ axis, and a graphical solution[1] shows that $k_c = 0.447\lambda$ and

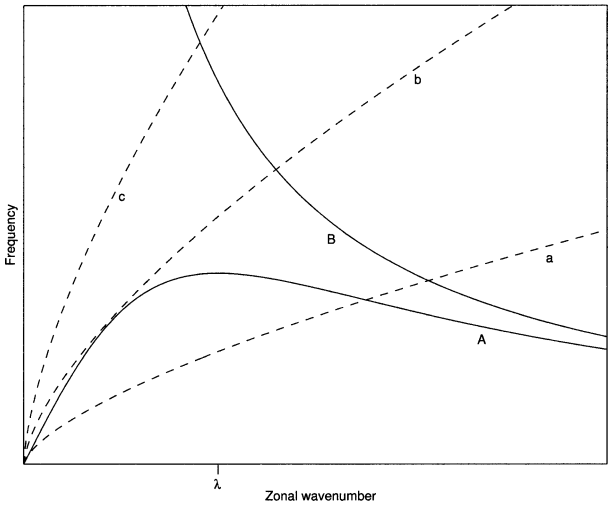

FIG. 1. Schematic graphs of Rossby wave frequencies and turbulent straining rates as functions of zonal wavenumber. Solid lines show Rossby wave dispersion frequencies (2.7) with (a) zero and (b) nonzero deformation wavenumber λ. Dashed lines show straining rates (2.8) of various flux strengths. Intersections imply that an upscale cascade of energy in zonal wavenumber will be inhibited by Rossby waves. All three strain rates will yield anisotropic flow when dispersion is given by curve (A). If the dispersion is given by (B), then curve (a) will also lead to anisotropic flow, curve (b) will lead to marginally anisotropic flow, and curve (c) will lead to isotropic flow.

$$\beta_c = 1.5\mathcal{C}^{1/2}(\epsilon\lambda^5)^{1/3}. \tag{2.9}$$

Defining $\tilde{\beta} \equiv \beta(\epsilon\lambda^5)^{-1/3}$ and assuming $\mathcal{C} = 6.0$, this is

$$\tilde{\beta}_c = 3.9. \tag{2.10}$$

On a rotating planet, β decreases with latitude and $\lambda(\propto f)$ increases with latitude, which implies, for a fixed ϵ, a distinct maximum latitude at which jets might be able to form. The critical β of (2.10) will later be shown, under certain circumstances, to yield flows that are supercritical with respect to the inviscid Charney–Stern criterion (CS).

c. CSM theory: Zonal flow scale via Charney–Stern marginal criticality and total energy constraint

It is known that the jets that form in *numerical models* are marginally stable with respect to the CS. Despite the inconsistency of this fact with observations of flow on the giant gas planets, we might expect that the criterion (along with some other constraints) could be used to predict the scale and rms velocity of the supposed jets. In this subsection we derive zonal flow scales and velocities based on this assumption, and term the resulting theory CSM (Charney–Stern marginal stability).

If $\beta > \beta_c$, then energy will coalesce into zonal modes, and a cascade along the $k = 0$ axis will ensue (Chekhlov et al. 1996; Marcus et al. 2000; Huang et al. 2001; Smith et al. 2002). If no drag is present, the cascade will proceed all the way to the domain scale (Manfroi and Young 1999; Huang et al. 2001). The theory presented in this

[1] Let $x \equiv (k/\lambda)^{1/3}$ and $a \equiv \beta/(\mathcal{C}^{1/2}\epsilon^{1/3}\lambda^{5/3})$, so that the relevant equation for critical parameters is $ax = x^6 + 1$. A single intersection can only occur when $a = 1.57$, and for this value of a, $x = 0.765$.

subsection assumes that stable jets will form at the zonal wavenumber l_0 of marginal barotropic stability, determined by the vanishing of the mean potential vorticity gradient, namely

$$\frac{\partial \overline{q}}{\partial y} = \beta - \frac{\partial^2 \overline{u}}{\partial y^2} + \lambda^2 \overline{u} = 0.$$

Assuming the mean zonal velocity is given by $\overline{u} = u_0 \sin(ly)$,[2] we find the condition for marginal stability:

$$l_0^2 = \frac{\beta}{u_0} - \lambda^2. \tag{2.11}$$

For a real solution to exist, one must have $\beta/(u_0\lambda^2) > 1$. Determination of the zonal flow scale l_0 requires additionally a prediction for the zonal velocity u_0.

In order to estimate u_0, we use the prediction for the total energy (2.3) and, separately, a scaling for the partition between available potential, meridional kinetic, and zonal kinetic energies. We make the following two assumptions: 1) the ratio of the available potential (P) to kinetic (K) energy at a given wavenumber κ scales like the ratio of that wavenumber to the deformation wavenumber λ, that is, $P/K \simeq \lambda^2/l_0^2$; 2) since we are seeking a state in which we expect strong flow anisotropy to form, we assume the final circulation is primarily zonal, so that $u_0 \gg \langle v \rangle$, and the energy is coalesced around the meridional wavenumber l_0. So, expressing the total energy as the sum of kinetic and available potential parts, we can rewrite (2.3) as

$$\left(1 + \frac{\lambda^2}{l_0^2}\right)\frac{u_0^2}{2} \simeq \frac{\epsilon}{2r}. \tag{2.12}$$

Equations (2.11) and (2.12) can be solved simultaneously,[3] resulting in the solution

$$\tilde{l}_0^2 \simeq \frac{1}{2}[(1 + 4\tilde{\beta}^2\tilde{r})^{1/2} - 1], \tag{2.13}$$

where $\tilde{l}_0 = l_0/\lambda$. The rms zonal velocity is

$$\frac{\tilde{u}_0}{\tilde{\beta}} \simeq 2[(1 + 4\tilde{\beta}^2\tilde{r})^{1/2} + 1]^{-1}, \tag{2.14}$$

where $\tilde{u}_0 = u_0(\epsilon\lambda^{-1})^{-1/3}$. The solutions are exact—the approximate equality symbols in (2.13) and (2.14) result from the fact that (2.12) is an approximation. Note that $\tilde{u}_0/\tilde{\beta} = u_0\lambda^2/\beta$, and that the right-hand side of (2.14) never exceeds unity.

Note also that we have used an inviscid stability criterion. Niino (1982) suggests a modified stability criterion that includes a dependence on the drag r. This criterion may provide a more relevant assessment for the current model, but is difficult to apply to the cases considered here, and will not be pursued. In any case, the effects of drag are taken into account in the following theory.

d. SI theory: Zonal flow scale via spectral integration and total energy constraint

The problem with the above theory is that it restricts the energy in zonal modes to a scale and magnitude that satisfy CS stability. Because we want a scaling that can potentially apply to observed jets, we separate the issues of jet stability and zonal energy. After all, there is nothing to preclude energy coalescing on the zonal axis ($k = 0$ in spectral space) without forming stable jets. Arguing strictly from cascade dynamics, and knowing that energy cascades to a scale that is a combined function of β and drag (Huang et al. 2001; Smith et al. 2002), we should be able to derive a scale for the energy peak on the zonal axis (l_0). In this section we proceed as suggested, and term the resulting theory for zonal scale and energy as spectral integration (SI).

In regimes of strong anisotropy, the kinetic energy spectrum is dominated by spectrally steep contributions along the zonal axis (see, e.g., Chekhlov et al. 1996), roughly obeying the form

$$\mathcal{K}(k) = \mathcal{C}_\beta \beta^2 \kappa^{-5}, \tag{2.15}$$

where $\mathcal{K}$ is the spectrum of kinetic energy, defined such that

$$K = \int_0^\infty \mathcal{K}(\kappa)\, d\kappa.$$

Using a similar relation for the spectrum $\mathcal{A}$ of available potential energy, we know that

$$\mathcal{A}(\kappa) = \lambda^2 \kappa^{-2} \mathcal{K},$$

and so the total energy spectrum for anisotropic flows is (see, e.g., Merilees and Warn 1972)

$$\mathcal{E}(k) = \mathcal{C}_\beta \beta^2 \kappa^{-5}(1 + \lambda^2 \kappa^{-2}). \tag{2.16}$$

We can estimate the zonal flow scale by integrating (2.16) from l_0 to ∞, neglecting the $-5/3$ contribution below the anisotropy boundary, and setting the result equal to $\epsilon/2r$,

$$\int_{l_0}^\infty \mathcal{E}(\kappa)\, d\kappa = \mathcal{C}_\beta \beta^2 \left(\frac{l_0^{-4}}{4} + \frac{\lambda^2 l_0^{-6}}{6}\right) = \frac{\epsilon}{2r}.$$

[2] In making the assumption of a sinusoidal velocity profile, we have assumed all the zonal energy has accumulated in one wavenumber. This is of course not accurate: observed jets are asymmetric. Generally, eastward jets are strong and sharp while westward jets are wide and weak, implying a broadband spectrum of energy along the l axis in wavenumber space. More complex estimates for the zonal velocity profile would likely introduce nondimensional form factors into the above calculation, but would not change the basic scaling dependencies.

[3] Letting $x \equiv l_0^2/\lambda^2 > 0$ and $y = \beta/(u_0\lambda^2) > 0$ [and noting that $\beta^2 r/(\lambda^4 \epsilon) \equiv \tilde{\beta}^2 \tilde{r}$] gives the pair of equations $x = y - 1$ and $1/x = y^2/(\beta^2 \tilde{r}) - 1$. Elimination of x results in a cubic equation in y, which can be readily solved.

The solution[4] is given by the single positive real root of

$$\tilde{l}_0 = \left(\frac{\gamma}{3}\right)^{1/6}\left[\left(1 + \sqrt{1 - \frac{\gamma}{3}}\right)^{1/3} + \left(1 - \sqrt{1 - \frac{\gamma}{3}}\right)^{1/3}\right]^{1/2}. \quad (2.17)$$

The parameter $\gamma = \mathcal{C}_\beta \tilde{\beta}^2 \tilde{r}/2$ is positive, and the discriminant of the square root changes sign at $\gamma = 3$. However, when the discriminant becomes negative, the two factors within parentheses are complex conjugates of one another, and so their sum is real. The positive, real root of the equation is continuous across the critical parameter.

Given knowledge of the zonal flow scale, the rms zonal velocity can be found approximately (neglecting meridional velocities) by integrating the kinetic energy spectrum:

$$\frac{u_0^2}{2} \simeq \int_{l_0}^{\infty} \mathcal{K}(\kappa)\, d\kappa = \frac{\mathcal{C}_\beta \beta^2}{4} l_0^{-4}.$$

In terms of the nondimensional parameters already introduced,

$$\frac{\tilde{u}_0}{\tilde{\beta}} = \left(\frac{\mathcal{C}_\beta}{2}\right)^{1/2} \tilde{l}_0^{-2} \quad (2.18)$$

with $\tilde{l}_0$ given by (2.17). Equations (2.17) and (2.18) should be compared to (2.13) and (2.14). Based on estimates from Chekhlov et al. (1996), the constant $\mathcal{C}_\beta$ is about 0.2–0.4, so that $\mathcal{C}_\beta/2 \sim 0.1$–$0.2$, and the factor cannot be neglected. So in this case, γ is similar to the factor $\tilde{\beta}^2\tilde{r}$ that appears in (2.13) and (2.14) of the CSM theory, but differs by the nondimensional prefactor $\mathcal{C}_\beta/2$.

In the small- and large-γ limits, expressions (2.17) and (2.18) take on simpler forms. Specifically,

$$\tilde{l}_0 = \begin{cases} (2\gamma/3)^{1/6}, & \gamma \ll 1 \\ (4\gamma/3)^{1/4}, & \gamma \gg 1, \end{cases} \quad \text{and} \quad (2.19)$$

$$\frac{\tilde{u}_0}{\tilde{\beta}} = \left(\frac{\mathcal{C}_\beta}{2}\right)^{1/2} \begin{cases} \left(\dfrac{2\gamma}{3}\right)^{-1/3}, & \gamma \ll 1 \\ \left(\dfrac{4\gamma}{3}\right)^{-1/2}, & \gamma \gg 1. \end{cases} \quad (2.20)$$

The error incurred by using the small-γ limit of (2.19) when $\gamma = 1$ is about 20%, and about 10% for the large-γ limit. An order of magnitude increase or decrease in γ reduces the error to less than 1% for each estimate, respectively.

e. Limitations imposed by drag

The above solutions assume that energy can cascade freely along the meridional wavenumber axis until it is halted by the combined β–r scale in (2.13) or (2.17), but if surface drag is large enough, the cascade will never reach scales where β becomes important. In the absence of β, drag itself can halt the cascade isotropically at the scale given by (2.6). On the other hand, for large enough β, the flow will be anisotropic with, perhaps, a zonal flow scale determined by one of the above theories. For CSM theory we can find the critical value of drag r_c such that, for $r > r_c$, no anisotropy will form and the cascade will peak isotropically at κ_r. To do this, we set κ_r in (2.6) to l_0 in (2.13). For SI theory, we can proceed similarly with the approximations in (2.19).

For CSM theory the physical solution[5] consists of two positive, real roots, for all $\beta \geq \alpha^{1/2}(27/4)^{1/6} \simeq 2.6$, which is smaller than the critical value of β required for anisotropy to form, given by (2.10). With $\beta = \beta_c \simeq 3.9$, values of the drag r that are either too small or too large will lead to isotropic flow. For higher values of β (e.g., $\beta = 5\beta_c$), the intersections move to extremely small and large values of γ, respectively, and so the zonal flow scale predicted by (2.13) is always smaller than the drag-induced scale (2.6) for physically reasonable values of γ. Anisotropy is thus always expected for moderately supercritical $\tilde{\beta}$.

For SI theory, we compare the approximations in (2.19) to (2.6). Setting the low-γ limit expression for $\tilde{l}_0$ in (2.19) equal to the drag scale κ_r in (2.6), we find a critical drag

$$\tilde{r}_c = \left(\frac{\mathcal{C}_\beta^4 \tilde{\beta}^8}{81\alpha^9}\right)^{1/5} \simeq (0.01)\tilde{\beta}^{8/5}.$$

Choosing $\beta = \beta_c$, the minimum value that will lead to anisotropy, gives us $\tilde{r}_c \simeq 0.1$ and $\gamma = 0.15$, validating a posteriori our small-γ assumption. Using the high-γ limit leads to a similar value. In simulations reported in the next section, drag never exceeds $\tilde{r} = 0.01$, or a tenth of the critical value at minimum β.

If drag or β is so large that the cascade peak scale is at or smaller than the deformation scale (an unphysical limit), then the drag scale (2.6) is no longer valid, since that scale is derived under the assumption that $\kappa \ll \lambda$. Rather, in the opposite limit $\kappa \gg \lambda$, we revert to two-dimensional vorticity dynamics and the appropriate isotropic halting scale is

$$\kappa_r = (\alpha_2 \tilde{r})^{3/2}. \quad (2.21)$$

However, this limit has no relevance to the current problem, since we are interested in scales $\kappa \sim l_0$, and all the physical systems to which the theory developed here might apply have jets at scales on order of or large compared to the deformation scale.

[4] Write the resulting equation as $x^3 - \gamma x - 2\gamma/3 = 0$, where $x = (l_0/\lambda)^2$ and $\gamma = \mathcal{C}_\beta \beta^2 r/(2\epsilon\lambda^4)$.

[5] Letting $x = (\alpha\tilde{r})^{1/4}$, solutions are the positive, real roots of $x^3 - (\tilde{\beta}^2/\alpha)x + 1 = 0$.

TABLE 1. Nondimensional parameters and their dimensional representations. The time and space scales used in nondimensionalization are given by (2.5).

Nondimensional parameter	Dimensional form
$\tilde{u}$	$u(\epsilon\lambda^{-1})^{-1/3}$
$\tilde{l}$	$l\lambda^{-1}$
$\tilde{\beta}$	$\beta(\epsilon\lambda^{5})^{-1/3}$
$\tilde{r}$	$r(\epsilon\lambda^{2})^{-1/3}$
γ	$(C_\beta/2)\beta^2 r\epsilon^{-1}\lambda^{-4}$
$\tilde{u}\tilde{\beta}^{-1}$	$u\lambda^2\beta^{-1}$

3. Numerical experiments

a. The numerical model

The simulations reported below were performed using a two-dimensional dealiased spectral model with 256^2 equivalent horizontal gridpoints ($\kappa_{\max} = 127$)—additionally, one simulation using 512^2 equivalent horizontal gridpoints was performed to demonstrate the robustness of the results with increasing resolution. The model uses a leapfrog time step to advance the solution, and a weak Robert filter to suppress the computational mode. The flow is forced with an isotropic random Markovian forcing at high wavenumber, typically $\kappa_F = 80$ ($\kappa_F = 160$ for the high-resolution run). Enstrophy is dissipated with a highly scale-selective exponential cutoff filter with explicitly vanishing dissipation below a cutoff wavenumber κ_{cut}. For simulations presented here, $\kappa_{\text{cut}} = \kappa_F + 5$. Traditional hyperviscosity, by contrast, dissipates at all scales. Even above the cutoff wavenumber, the dissipation level does not become significant until near the maximum wavenumber in the computational domain. Thus, while we focus here on maintaining as wide an inverse cascade range as possible, we have allowed a reasonable direct cascade for wavenumbers $\kappa > \kappa_F$. The small-scale dissipation, despite its presence only at $\kappa > \kappa_F$, removes some of the input energy. The model calculates this loss at each time step and uses it to set the magnitude of the forcing such that the *net* upscale energy transfer rate, after losses to the enstrophy filter, is fixed at $\epsilon = 1$. Appendix B of Smith et al. (2002) details the forcing function and enstrophy filter, with the exception that in the present paper, the forcing is altered (as explained in the previous sentence) to normalize the forcing completely, including for losses of energy to the enstrophy filter.

b. Summary of simulations and comparison to theories

We describe a set of simulations devised to test the relations derived in section 2. The results are described in terms of the nondimensional parameters defined in section 2, all of which are summarized in Table 1. Four series of simulations, along with a set of special or extreme cases, are reported and their parameters are described in Table 2. The simulation series vary β, deformation wavenumber (λ), and drag (r) with other parameters fixed. The fourth series varies drag at a different value of β than the first drag series. The four

TABLE 2. Model parameter values and steady-state results for the numerical simulations reported.

Run	λ	β	r	$\tilde{\beta}$	$\tilde{r}$	γ	$\tilde{l}_0$	$u_0\lambda^2/\beta$	$\lvert v\rvert/\lvert u\rvert$	Jets?
B1	20	800	0.02	5.40	2.70×10^{-3}	8.00×10^{-3}	0.504	1.23	0.892	No
B2		1.50×10^{3}		10.2		0.0280	0.530	0.764	0.521	Yes
B3		2.00×10^{3}		13.6		0.0500	0.579	0.619	0.445	Yes
B4		2.50×10^{3}		17.0		0.0780	0.626	0.529	0.400	Yes
B5		3.00×10^{3}		20.4		0.113	0.684	0.468	0.363	Yes
B6		4.00×10^{3}		27.1		0.200	0.720	0.388	0.290	Yes
B7		8.00×10^{3}		54.3		0.800	1.02	0.240	0.168	Yes
B8		1.50×10^{4}		102		2.82	1.39	0.139	0.140	Yes
B9		2.00×10^{4}		136		5.00	1.55	0.108	0.104	Yes
B10		4.00×10^{4}		271		20.0	1.77	0.0559	0.0726	Yes
L1	5	3.00×10^{3}	0.0200	205	6.80×10^{-3}	28.8	1.94	0.0754	0.161	Yes
L2	10			64.6	4.30×10^{-3}	1.80	1.15	0.259	0.193	Yes
L3	30			10.4	2.10×10^{-3}	0.0220	0.479	1.223	0.494	Yes
L4	40			6.41	1.70×10^{-3}	7.00×10^{-3}	0.404	1.764	0.740	?
L5	60			3.26	1.30×10^{-3}	1.40×10^{-3}	0.272	3.274	0.940	No
RA1	20	3.00×10^{3}	0.0100	20.4	1.40×10^{-3}	0.0563	0.557	0.551	0.345	Yes
RA2			0.0500		6.80×10^{-3}	0.281	0.746	0.352	0.426	Yes
RA3			0.100		0.0136	0.563	0.917	0.296	0.470	Yes
RA4			0.200		0.0271	1.13	1.21	0.240	0.555	Yes
RB1	20	8.00×10^{3}	0.0100	54.3	1.40×10^{-3}	0.400	0.957	0.319	0.134	Yes
RB2			0.0500		6.80×10^{-3}	2.00	1.33	0.175	0.230	Yes
RB3			0.100		0.0136	4.00	1.55	0.130	0.313	Yes
LG	80	6.00×10^{-3}	0.0100	4.04	5.39×10^{-4}	8.80×10^{-4}	0.176	2.03	0.821	?
NV	20	3.00×10^{3}	0.0200*	20.4	2.70×10^{-3}	0.113	0.553	0.470	0.356	Yes

* Drag was applied only to the vortex-stretching for run NV.

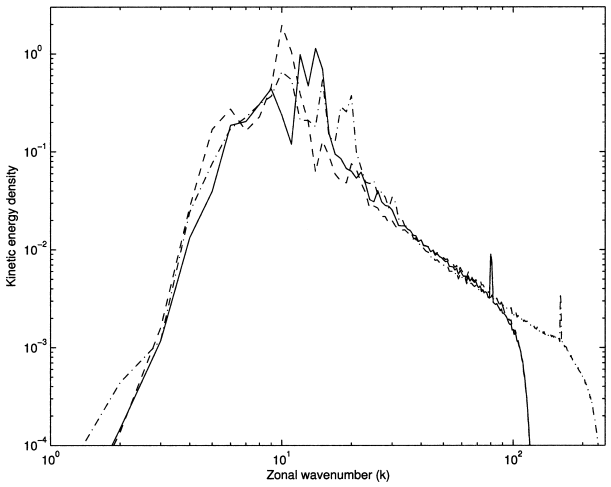

FIG. 2. Comparison of kinetic energy spectra for simulations B5 (solid), NV (dashed), and HR (dashed–dotted). Simulation HR uses the same parameters as B5 but with twice the numerical resolution and forcing dissipation cutoff scales half as large as for B5. Simulation NV uses the same parameters as B5, but with no drag applied to the vorticity.

series will be referred to as the B series, L series, RA series, and RB series, respectively. The special cases consist of one run with a set of parameters chosen to give a very small value of γ (called LG), one simulation in which the linear drag is applied only to the vortex stretching term (i.e., thermal drag without vorticity drag: NV for ''no vorticity drag''), and one simulation performed at twice the resolution (HR for ''high resolution''). The latter two special cases were performed using parameters identical to the simulation labeled B5, the canonical simulation. Smaller values than $r = 0.01$ were not performed because the number of time steps required to reach a statistically steady state grows inversely with the drag, and the lowest drag simulations performed required millions of time steps in some cases.

The parameters for simulation LG were chosen to investigate a lower, but still numerically realizable value of γ at which anisotropy might still form. The limitations are that β is large enough for anisotropy to form; drag is small enough that it does not control the inverse cascade; and that drag is not too small, so that numerical equilibration is attainable in reasonable time. The values of the parameters used are listed in Table 2. Note that $\tilde{\beta}$ is only slightly larger than $\tilde{\beta}_c = 3.9$, and so the flow should be barely supercritical for anisotropy formation.

In order to ensure that our results are not dependent on resolution, simulation HR was performed using identical parameters to simulation B5, but with twice the resolution and half the forcing scale. A comparison of the resulting kinetic energy spectra is shown in Fig. 2 (along with a comparison to simulation NV, discussed later). The total energy in the two simulations is within 5%, as are the derived zonal flow scale and rms zonal velocity. We conclude that the results are not dependent on resolution.

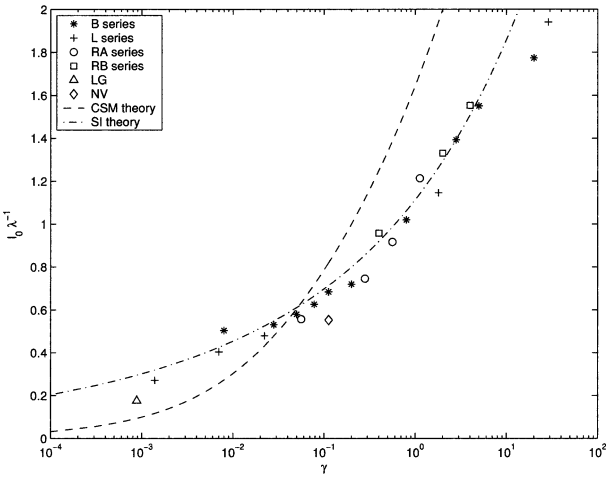

FIG. 3. Nondimensional energy peak wavenumber $\tilde{l}_0 = l_0\lambda^{-1}$ vs $\gamma = (C_\beta/2)\beta^2 r\epsilon^{-1}\lambda^{-4}$. The simulated peak meridional wavenumber l_0 is calculated as the centroid of a slice of the time-averaged kinetic energy spectrum along the y axis, which is a very steep spectrum (-6) and so gives a good statistical indication of the spectral peak. The CSM theory prediction (2.13) is plotted as a dashed line, and the SI theory prediction (2.17) is plotted as a dashed–dotted line. The parameter value $C_\beta = 0.2$ is used for all calculations.

Figures 3 and 4 show the compiled nondimensional energy peak scales and rms zonal velocities for all the simulations performed, plotted as functions of γ. A value of $C_\beta = 0.2$ was used in calculating γ for the simulations performed. The peak meridional wavenumber l_0 is calculated as the centroid of a slice of the time-averaged kinetic energy spectrum along the y axis,

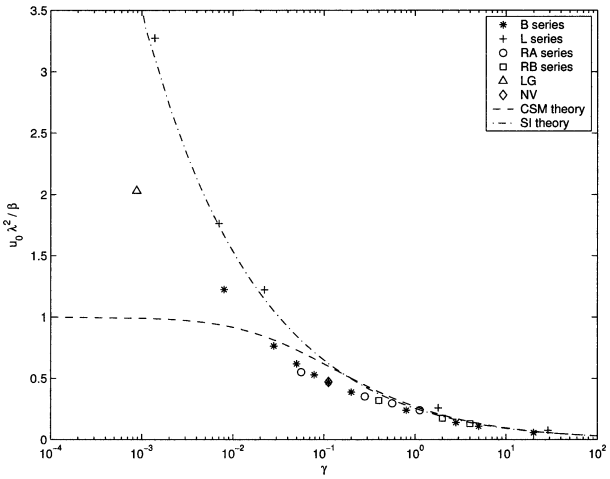

FIG. 4. Nondimensional jet velocity $\tilde{u}_0\tilde{\beta}^{-1} = u_0\lambda^2\beta^{-1}$ vs γ (defined in the caption of Fig. 3). The nondimensional jet velocity must be less than unity to satisfy the inviscid CS condition [see (2.11)]. The simulated jet velocity u_0 is calculated as the square root of twice the total time-averaged kinetic energy, and hence assumes that the meridional velocity is negligible. The CSM theory prediction (2.14) is plotted as a dashed line and the SI theory prediction (2.18) is plotted as a dashed–dotted line. The deviations at small γ are due to the weak anisotropy of the flow, which is not accounted for by either theory. The parameter value $C_\beta = 0.2$ is used for all calculations.

which is a very steep spectrum (-6) and so gives a good statistical indication of the spectral peak. The rms zonal velocity u_0 is calculated as the square root of twice the total time-averaged kinetic energy, and hence assumes that the meridional velocity is negligible. The values plotted, as well as the anisotropy (defined as the ratio of rms meridional to zonal velocities) for each run are also tabulated in Table 2. The theories from sections 2c and 2d are plotted along with the model output. CSM theory is plotted as a function of γ by substituting $2\gamma/C_\beta$ for $\tilde{\beta}^2\tilde{r}$ in (2.13) and (2.14).

The model output for the peak meridional energy scale in Fig. 3 is clustered along the prediction of SI theory for the whole range of γ considered, with the greatest variations for simulations LG, B10, and L1. Error bars generated from the model data would be smaller than the size of the symbols in the plot, and so are not displayed. In any case, both ''theories'' are far from exact, and so exact correspondence is not expected. A major error, for example, is that for runs with $\tilde{\beta}$ close to the critical value, the flow is not highly anisotropic, and so meridional velocities cannot be neglected. Considering Fig. 4, the deviations from data at small γ are due to the weak anisotropy of the flow, which is not accounted for by either theory. The close correspondence of the L series simulations with SI theory at small γ is surprising. The trends of the output are nevertheless sufficiently consistent with the scale predictions for SI theory to rule out CSM theory as a predictor for the flow scale.

Note that while γ varies over 4 decades, the ratio of zonal flow scale to deformation scale varies only between about 3.0 and 0.5, the former occurring for very small γ. Apparently, it is very difficult to form zonal flow scales, much less stable jets, that are much larger than the deformation scale. This is consistent with the observed near coincidence of the two scales on Jupiter and Saturn.

c. Jet stability versus flow anisotropy

The model data for the rms zonal velocity in Fig. 4 is plotted as $\tilde{u}_0/\tilde{\beta} = u_0\lambda^2/\beta$, which is just the supercriticality for CSM theory (the CS criterion). Note that the curve for CSM theory asymptotes to unity at small γ, consistent with the constraint (2.11) used to derive it. The model output, however, clearly does not obey this constraint, and again is more consistent with the SI theory.

The physical space zonal velocity fields for L series runs and for run LG are shown in Fig. 5 and those for the first six B series runs (B1–B6) in Fig. 6. The purpose of these figures is to assess the flows for the presence of stable jet structures, so no scale is given on the plots. Simulations L3, L4, L5, LG, B1, and marginally B2 have rms zonal velocities exceeding the CS limit (see Fig. 4). Nevertheless, only those with $\tilde{\beta} \lesssim 4$ (B1, L5, LG) show almost no sign of jets. Simulations B2, L4, and L3 all show jet structure, despite that they violate the CS criterion, but the jets are very wiggly and broken in some places. Indications for the presence of jets are tabulated in the final column of Table 2.

One can infer from the results that it is appropriate to separate the issues of jet stability and flow anisotropy. The latter is controlled by the steady-state spectral distribution of turbulent energy, while the former surely depends on the relevant stability criterion for the flows at hand. For example, Dowling (1994) argues that jets on Jupiter are critically stable with respect to Arnold's Second Stability criterion. Ingersoll and Pollard (1982), by contrast, claim that a Charney–Stern criterion modified for deep flows characterizes Jovian jets. More recently Galperin et al. (2001) pointed out that any stability criterion should include drag. Most basically, McIntyre and Shepherd (1987) show that even periodicity in the meridional (y) direction, or the lack thereof, can affect the relevant stability criteria. In any case, none of these approaches determine the energy level of anisotropic flow, but rather only the ability for stable jets to form given the generation of anisotropic energy.

d. Thermal drag versus vorticity drag

The restriction that the drag on the system be applied to both the stretching and vorticity, and be equal, is too restrictive to be directly applicable to physical systems. However, in systems with large-scale (compared to the deformation scale) jets, the available potential energy will dominate, and so the thermal drag should accomplish most of the dissipation. Simulation NV was performed as a test for this limit. The parameters used for this simulation are identical to simulation B5 except that no drag is applied to the vorticity (the extreme case). Explicitly, decomposing the drag term from (2.1),

$$rq = r_\zeta\nabla^2\psi - r_\psi\lambda^2\psi,$$

we have set $r_\zeta = 0$ in simulation NV, while in all other simulations we have set $r_\zeta = r_\psi = r$. The results for the scale and velocity of zonal flow are displayed with a diamond in Figs. 3 and 4. The zonal velocity is nearly identical for the two runs, while the zonal scale is larger in simulation NV than in B5. While the kinetic energy is nearly the same in the two runs, the available potential energy in NV is 35% higher. One might have expected the reverse to occur, given that vorticity drag damps kinetic energy while thermal drag damps potential energy. Instead, the lack of vorticity drag has allowed the inverse cascade to proceed to slightly larger scale, and this change in scale is reflected more dramatically in the potential energy spectrum, which is amplified at large scale and reduced at small scale by the factor λ^2/κ^2. A comparison of the kinetic energy spectra for simulations B5 and NV is shown in Fig. 2. The change in zonal scale in the absence of vorticity drag is a weakness of the theory.

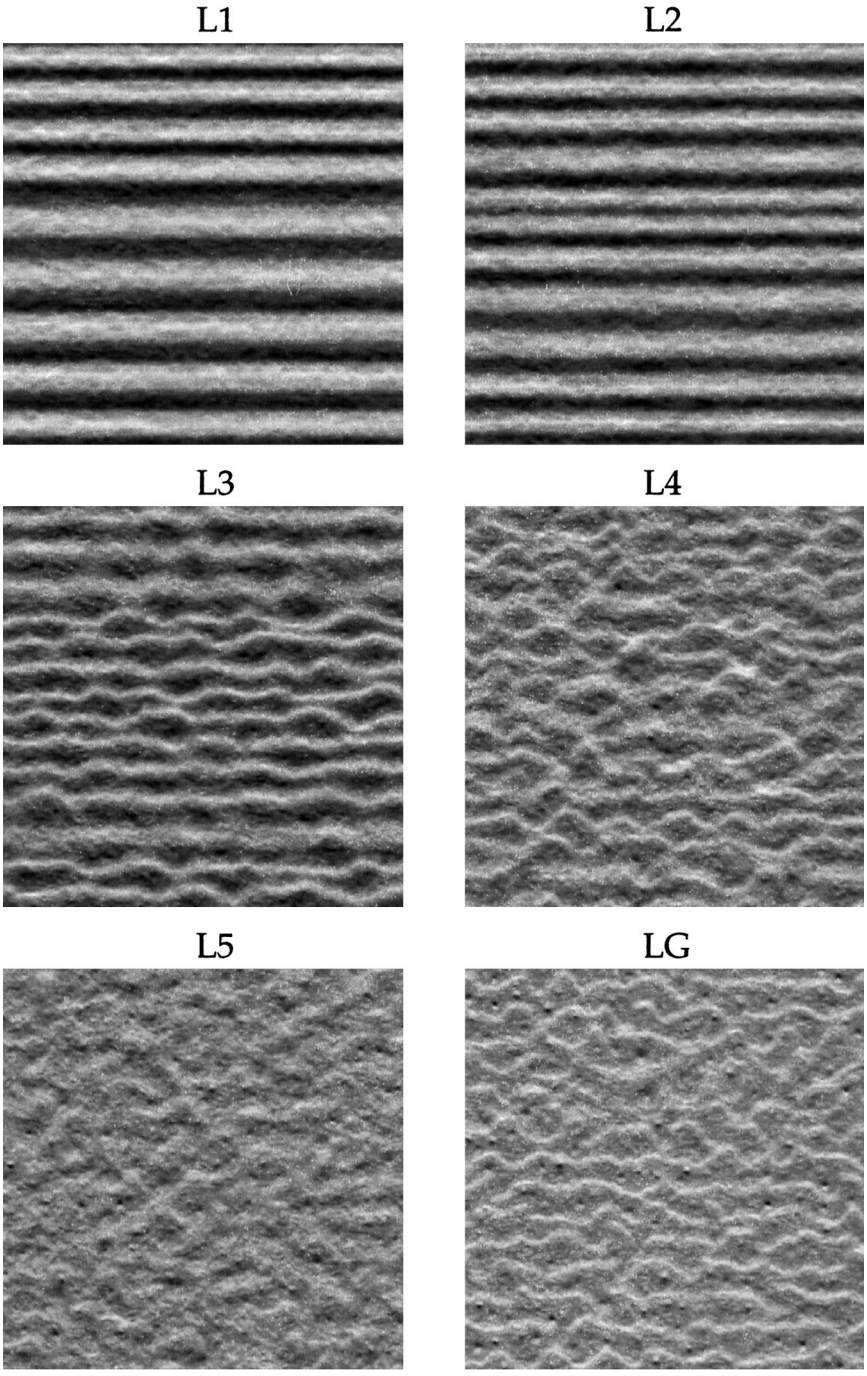

FIG. 5. Instantaneous zonal velocity fields for L series and LG simulations. These figures demonstrate the presence and absence of jets in various simulations (no scale is necessary). See text and Table 2.

4. Application to Jupiter and Saturn

The theories presented can be applied directly to limited aspects of the observed zonal wind data for the giant gas planets. However, their simplicity and limitations must be taken into account, and resulting predictions restricted to their regimes of validity. The theoretical framework presented considers only barotropic vorticity dynamics, and will not be relevant too close to the equator. Second, apart from the overall forcing level, details of the convective forcing are not represented. Third, the homogeneous nature of the theories

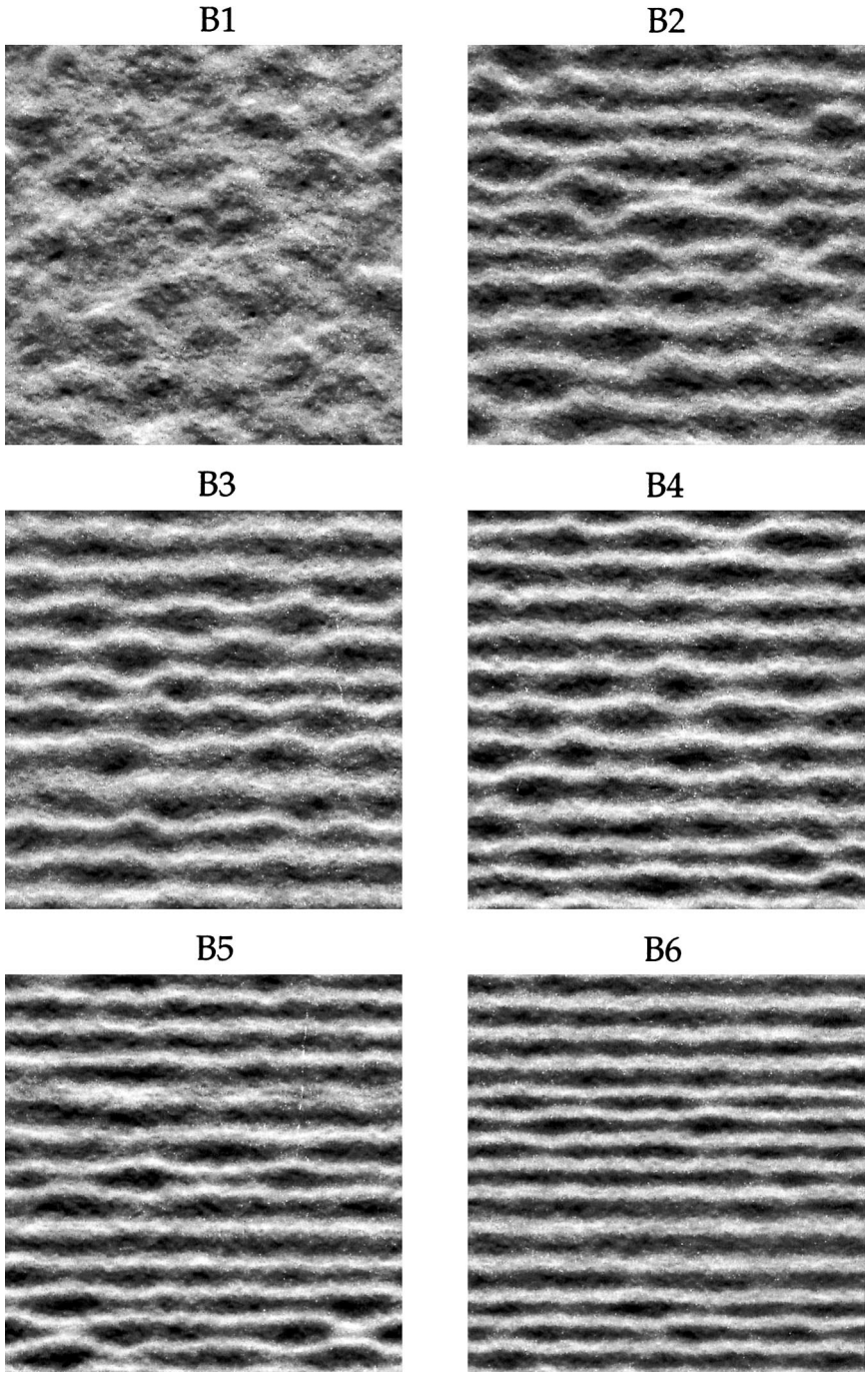

FIG. 6. Instantaneous zonal velocity fields for first six B series simulations. Comments in caption to Fig. 5 apply.

precludes the prediction of jet directions and asymmetries. Nevertheless, both theories can be tested against the observed scale and speed of the zonally averaged profiles of those jets beyond the equatorial zone. Equation (2.9) also predicts latitudes above which jets should not form.

In order to apply SI theory to planetary data, five physical parameters must be specified: the rotation rate Ω, the planetary radius a, the deformation wavenumber λ, the convective energy generation rate ϵ, and the drag r. Here, the theory will be applied to the zonal winds on Jupiter and Saturn, the known planetary parameter values for which are given in Table 3. The planet radii and rotation rates are well known, and Allison (2000)

TABLE 3. Planetary data for Jupiter and Saturn. Estimates of gravity wave speed are from Allison (2000) and estimates of generation and drag for Jupiter are from Galperin et al. (2001).

Parameter	Jupiter	Saturn
Planet radius (a)	7.15×10^7 m	6.03×10^7 m
Planet rotation rate (Ω)	1.76×10^{-4} s^{-1}	1.64×10^{-4} s^{-1}
Gravity wave speed (NH)	$\sim$700 m s^{-1}	$\sim$1500 m s^{-1}
Eddy generation (ϵ)	$\sim 10^{-7}$ m^2 s^{-3}	?
Drag (r)	$\sim 3 \times 10^{-12}$ s^{-1}	?

provides estimates of the product of stratification and scale height from gravity wave speed observations. From these, one can estimate the deformation wavenumber as

$$\lambda(\phi) \simeq \frac{4\pi\Omega}{NH} \sin(\phi), \tag{4.1}$$

where ϕ is the latitude. The Coriolis gradient is

$$\beta(\phi) = \frac{2\Omega}{a} \cos(\phi), \tag{4.2}$$

Galperin et al. (2001), using data from Gierasch et al. (2000), given an estimate of the energy flux ϵ for Jupiter from convective stirring, and also estimate the drag time scale (the low end of their estimate is quoted in Table 3). No estimates of the latter two values are known for Saturn.

Figure 7a plots the maxima of Jovian eastward jet velocities and velocity errors versus absolute planetographic latitude from García-Melendo and Sánchez-Lavega (2001) data, shown as squares for Northern Hemisphere jets and circles for Southern Hemisphere jets. The solid line is the prediction from SI theory (2.18) using the parameter estimates described above, and the dashed line is the equivalent prediction using CSM (2.14). As it was with the simulation data, the nondimensional value $\mathcal{C}_\beta = 0.2$ is used for the SI theory prediction. (Latitudinal estimates for the Jovian values of γ and $\tilde{\beta}$ that result from the parameter estimates are shown as solid lines in Fig. 9.) Apart from the anomalously sharp and intense jet at 23°N, SI theory lies within the scatter of the data, while CSM greatly underpredicts jet speeds at all latitudes.

Figure 7b plots the the meridional scale of the zonally averaged zonal wind for Jupiter against the predictions of SI theory (2.17) (solid line) and CSM theory (2.13) (dashed line). The scale analysis is based on the full profile of Jovian zonally averaged zonal wind from García-Melendo and Sánchez-Lavega (2001), and is explained in the appendix. The results for the scale analysis show a more striking departure between theories than for jet speeds. The SI theory roughly fits the data, and when the variation of deformation scale and β are taken into account, SI theory predicts an increase in jet scale toward the equator, but nearly constant scales at midlatitudes, as observed. CSM theory, by contrast, is absolutely inconsistent with the data. The CSM prediction (dashed) increases to tenfold larger jets than observed at midlatitudes (exceeding the plot axes).

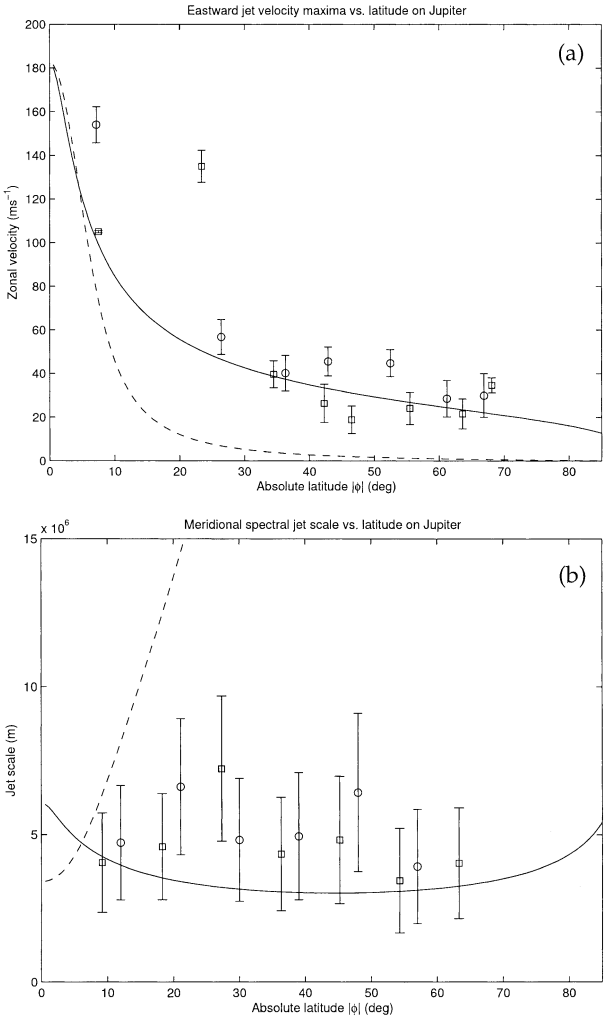

FIG. 7. (a) Eastward jet velocity maxima and (b) meridional spectral jet scale vs absolute planetographic latitude for Jupiter. The solid lines are estimates from SI theory [(2.18) and (2.17)] using values parameters given in Table 2, and the dashed lines are the estimates from CSM theory [(2.14) and (2.13)] using the same parameter values. The data points and error bars are from García-Melendo and Sánchez-Lavega (2001). Squares denote Northern Hemisphere points, and circles denote Southern Hemisphere points. See text for explanation of scale analysis.

Figure 8 is similar to Fig. 7, but uses the data of Sánchez-Lavega and Rojas (2000) for Saturn's zonally averaged zonal wind. The theoretical estimates for the Saturnian flow, however, require parameter values for which no published estimates exist, as mentioned above. Without further guidance, drag is estimated to be the same as that for Jupiter, while the convective generation rate ϵ is *adjusted to fit the data.* A value of $\epsilon \sim 10^{-6}$ m^2 s^{-3} is found to best fit the jet speed maxima data with SI theory. The requisite latitudinal estimates for the values of γ and $\tilde{\beta}$ for Saturn based on this value are shown as the dashed lines in Fig. 9. The SI and CSM curves in

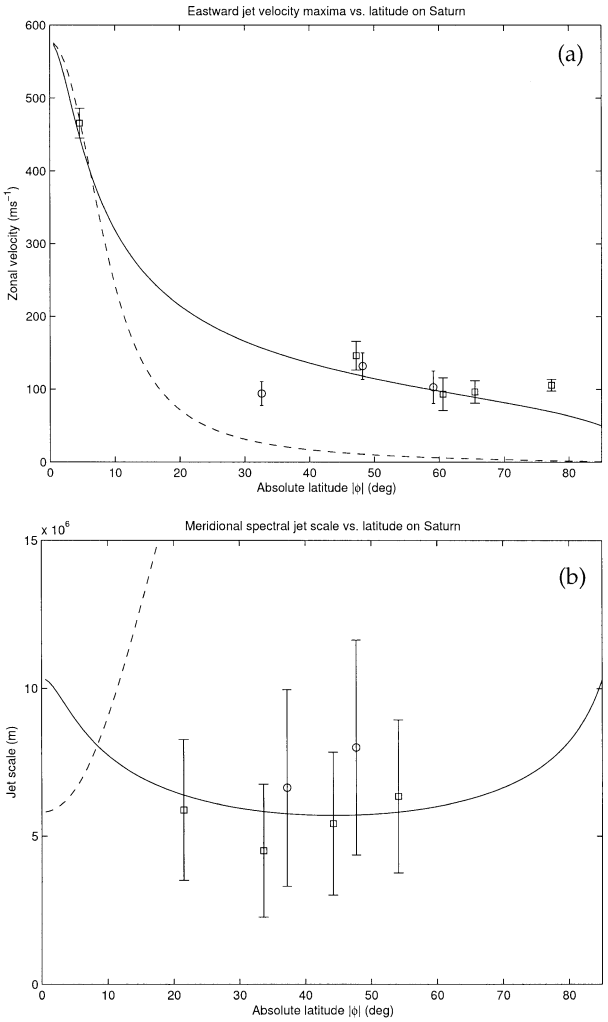

FIG. 8. Same as Fig. 7, except that no independent estimates for the drag and convective generation rate on Saturn exist. The drag is estimated to be the same as that for Jupiter, and the convective forcing rate ϵ is chosen to give the best fit to the data. The value found is 10 times the value estimated for Jupiter. See Fig. 9 for the resulting estimates of γ and β. The data points and error bars are from Sánchez-Lavega and Rojas (2000).

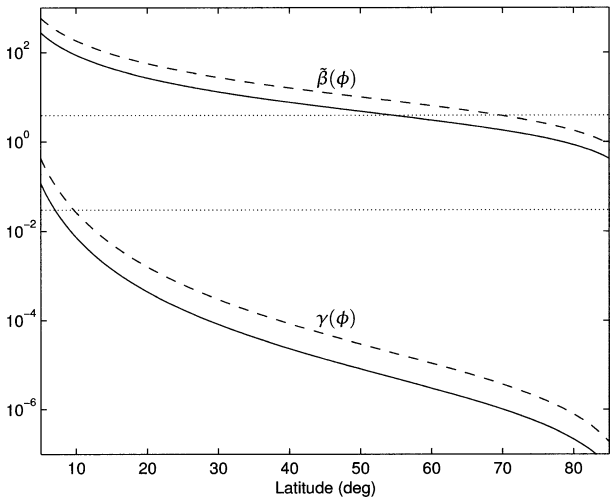

FIG. 9. Estimated values for $\tilde{\beta}$ and γ as functions of latitude for Jupiter (solid) and Saturn (dashed). Horizontal lines denote critical values for β ($\beta > 3.9$ implies anisotropic flow) and γ ($\gamma < 3 \times 10^{-2}$ implies flow will be supercritical with respect to the inviscid Charney–Stern criterion).

Fig. 8 for both jet speed (Fig. 8a) and scale (Fig. 8b) use the resulting values of γ.

In Fig. 9, note that $\tilde{\beta} > 3.9$ for latitudes up to about 55° on Jupiter, and latitudes up to about 70° on Saturn. Actual jets do exist at latitudes higher than these predicted critical latitudes, but do fail to form at polar latitudes. Also note that γ is very small in the midlatitudes on both planets, implying CS supercritical zonal energies and scales (this is implied for all $\gamma \lesssim 3 \times 10^{-2}$), consistent with observations.

5. Discussion

We have investigated a geometrically simple but parametrically complex representation of forced and dissipated turbulence as a local model for flow in rotating, stratified atmospheres driven by small-scale convective stirring. The new and interesting aspect of the present work is the simultaneous inclusion of β, a finite deformation scale and large-scale drag in a model stirred by small-scale random forcing. The linear drag is arguably the weakest aspect of the investigation, but provides a constraint on the overall flow energy, removing a major uncertainty.

The first result is that, in order for the flow to become anisotropic, β must exceed a critical value that is a function of the local deformation scale and the eddy energy generation rate (2.10). This condition is not equivalent to a stability criterion, but rather determines whether large-scale meridional flow is inhibited. When conditions are favorable for the production of anisotropy, the energy constraint imposed by the drag, in conjunction with the Rhines–Chekhlov spectrum (2.15) and the partition between kinetic and potential energy, predicts the steady-state zonal flow scale and rms velocity with some accuracy. This theory was referred to as SI theory and was compared to an alternate candidate that used the inviscid Charney–Stern criterion as a predictor for jet scale. A wide range of numerical simulations were performed and demonstrate that the former theory is consistent with the results of the simulations while the latter is not. The implication is that zonal energy levels and scales that would be supercritical to the CS condition, were they to form into jets, can be generated.

The formation of stable jets is another matter, and likely depends on the geometry of the flow. Anisotropy is shown to form without stable jets in inviscid CS supercritical parameter regions, though additionally we find that semistable supercritical jets can be formed even with our simple doubly periodic spectral model. In any

case, it is clear that marginal barotropic stability does not predict the presence, scale, or strength of turbulent anisotropic flow.

Despite the simplicity of the theory, we find that, as a local model, its predictions bear quantitative resemblance to the observed jet scales and strengths on Jupiter. The SI theory predicts that meridional jet scale should be roughly constant in midlatitudes but increase in scale toward the equator, and that jets should cease to form toward the poles, all as observed. The prediction for the latitudinal distribution of jet speeds and scales on Jupiter is moreover consistent with the data in some detail. Application of the theory to Saturn required choosing a convective forcing rate 10 times that on Jupiter to best fit the data. Varying this single parameter, however, yields predictions for the latitudinal distribution of jet speeds and scales that are consistent with Saturnian data in detail, notably predicting the observed twofold larger jet scales and fourfold faster jet speeds observed there relative to Jupiter. It will be interesting to see whether future observations yield measurements consistent with this prediction for convective forcing on Saturn. The combination of model simplicity and parameter data incompleteness makes this the roughest of comparisons. Nevertheless, the presented theory provides a relatively simple explanation for the most basic features of the observed midlatitude zonal wind profiles on the gas planets.

Acknowledgments. The author thanks the three reviewers of this paper for their careful analysis and constructive comments, all of which led to an improved paper. Some of the simulations reported here were computed on the supercomputing facilities at NOAA's Geophysical Fluid Dynamics Laboratory.

APPENDIX

Analysis of Meridional Scale Zonal Wind Data

In order to extract the scale of the jets as a function of latitude, as shown in Figs. 7b and 8b, a sliding windowed (or ''short time'') fast Fourier transform (FFT) is calculated at each latitude, starting and ending at latitudes where the data begins and ends, less one half the width of the window. The scales are then calculated as $2\pi/\kappa_c$, where κ_c is the centroid wavenumber of each FFT density spectrum. Error bars are taken as one half the second moment of each spectrum. Points are plotted for each half window width, so that windowed data overlaps. Northern and Southern Hemisphere data is staggered to allow for clarity in the plot.

Window widths are chosen large enough to resolve the full widths of jets (outside the Tropics) but small enough to allow for a sufficient range of scale calculations to demonstrate the latitudinal variation of the results. A range of window widths can be used, but must be chosen to balance spectral resolution against spatial resolution (the larger the window, the better the FFT, but the narrower the range of latitudes for which scales can be calculated). Within the usable and meaningful range of possible window widths, the results do not vary significantly.

For the Jovian Northern Hemisphere, the García-Melendo and Sánchez-Lavega (2001) data consists of 256 velocity values at evenly spaced latitudes ranging from 0.3° to 76.7°. An 18° window width was used for the Northern Hemisphere data and scales are plotted from overlapping windowed regions whose centers are spaced 9° apart.

Jovian Southern Hemisphere data from García-Melendo and Sánchez-Lavega (2001) consists of 226 velocity values at evenly spaced latitudes ranging from $-0.3°$ to $-67.8°$. The same window width and spacing of plotted scales as for the Northern Hemisphere data is used, but they are offset by 3° to allow separation from the Northern Hemisphere scale points.

The same analysis is made of the Saturnian data found in Sánchez-Lavega and Rojas (2000). The Saturnian Northern Hemisphere data consists of 155 velocity values at *nearly* evenly spaced latitudes ranging from 0° to 80.7°. A larger window width of 41.7° was necessary both to resolve the larger jet widths, and to give sufficient resolution to the FFTs, given the smaller number of data points. Scale points are plotted at separations of 11°.

The Saturnian Southern Hemisphere data consists of 102 velocity values that are nearly evenly spaced for latitudes ranging from $-10.7°$ to $-70.9°$. Data exists for the equatorward latitudes $-1°$, $-1.5°$, and $-2.1°$, but data for latitudes between $-2.1°$ and $-10.7°$ is unavailable because they are obscured by Saturn's rings. Window widths of 62.7° were necessary to produce useful results. The scale points are plotted at a separation of 11°.

REFERENCES

Allison, M., 2000: A similarity model for the windy Jovian thermocline. *Planet. Space Sci.*, **48,** 753–774.

Borue, V., 1994: Inverse energy cascade in stationary two-dimensional homogeneous turbulence. *Phys. Rev. Lett.*, **72,** 1475–1478.

Chekhlov, A., S. A. Orszag, S. Sukoriansky, B. Galperin, and I. Staroselsky, 1996: The effect of small-scale forcing on large-scale structures in two-dimensional flows. *Physica D,* **98,** 321–334.

Cho, J. Y.-K., and L. M. Polvani, 1996: The emergence of jets and vortices in freely evolving, shallow-water turbulence on a sphere. *Phys. Fluids,* **8,** 1531–1552.

Danilov, S., and D. Gurarie, 2001: Nonuniversal features of forced two-dimensional turbulence in the energy range. *Phys. Rev.*, **63E,** doi:10.1103/PhysRevE.63.020203.

Dowling, T. E., 1994: Successes and failures of shallow-water interpretations of voyager wind data. *Chaos,* **4,** 213–225.

Galperin, B., S. Sukoriansky, and H. P. Huang, 2001: Universal n^{-5} spectrum of zonal flows on giant planets. *Phys. Fluids,* **13,** 1545–1548.

García-Melendo, E., and A. Sánchez-Lavega, 2001: A study of the stability of Jovian zonal winds from HST images: 1995–2000. *Icarus,* **152,** 316–330.

Gierasch, P. J., and Coauthors, 2000: Observations of moist convection in Jupiter's atmosphere. *Nature,* **403,** 628–630.

Grianik, N., I. M. Held, K. S. Smith, and G. K. Vallis, 2004: The effects of quadratic drag on the inverse cascade of two-dimensional turbulence. *Phys. Fluids,* **16,** 1–16.

Huang, H. P., B. Galperin, and S. Sukoriansky, 2001: Anisotropic spectra in two-dimensional turbulence on the surface of a rotating sphere. *Phys. Fluids,* **13,** 225–240.

Ingersoll, A. P., and D. Pollard, 1982: Motion in the interiors and atmospheres of Jupiter and Saturn: Scale analysis, anelastic equations, barotropic stability criterion. *Icarus,* **52,** 62–80.

——, and Coauthors, 2000: Moist convection as an energy source for the large-scale motions in Jupiter's atmosphere. *Nature,* **403,** 630–632.

Kukharkin, N., and S. A. Orszag, 1996: Generation and structure of Rossby vortices in rotating fluids. *Phys. Rev.,* **54E,** 4524–4527.

Maltrud, M. E., and G. K. Vallis, 1991: Energy spectra and coherent structures in forced two-dimensional and beta-plane turbulence. *J. Fluid Mech.,* **228,** 321–342.

Manfroi, A. J., and W. R. Young, 1999: Slow evolution of zonal jets on the beta plane. *J. Atmos. Sci.,* **56,** 784–800.

Marcus, P. S., T. Kundu, and C. Lee, 2000: Vortex dynamics and zonal flows. *Phys. Plasmas,* **7,** 1630–1640.

McIntyre, M. E., and T. G. Shepherd, 1987: An exact local conservation theorem for finite-amplitude disturbances to non-parallel shear flows, with remarks on Hamiltonian structure and on Arnol'd's stability theorems. *J. Fluid Mech.,* **181,** 527–565.

Merilees, P. E., and T. Warn, 1972: The resolution implications of geostrophic turbulence. *J. Atmos. Sci.,* **29,** 990–991.

Niino, H., 1982: A weakly non-linear theory of barotropic instability. *J. Meteor. Soc. Japan,* **60,** 1001–1023.

Okuno, A., and A. Masuda, 2003: Effect of horizontal divergence on the geostrophic turbulence on a beta-plane: Suppression of the Rhines effect. *Phys. Fluids,* **15,** 56–65.

Sánchez-Lavega, A., and J. F. Rojas, 2000: Saturn's zonal winds at cloud level. *Icarus,* **147,** 405–420.

Smith, K. S., G. Boccaletti, C. C. Henning, I. N. Marinov, C. Y. Tam, I. M. Held, and G. K. Vallis, 2002: Turbulent diffusion in the geostrophic inverse cascade. *J. Fluid Mech.,* **469,** 13–48.

Vallis, G. K., and M. E. Maltrud, 1993: Generation of mean flows and jets on a beta plane and over topography. *J. Phys. Oceanogr.,* **23,** 1346–1362.

Williams, G. P., 1978: Planetary circulations: 1. Barotropic representation of Jovian and terrestrial turbulence. *J. Atmos. Sci.,* **35,** 1399–1426.